ACS OMEGA

Article

Cite This: ACS Omega 2019, 4, 15567−15580

http://pubs.acs.org/journal/acsodf

Nanobubble Liposome Complexes for Diagnostic Imaging and Ultrasound-Triggered Drug Delivery in Cancers: A Theranostic Approach

Ameya Prabhakar and Rinti Banerjee*

Department of Biosciences and Bioengineering, Indian Institute of Technology Bombay, Mumbai 400076, India

Supporting Information

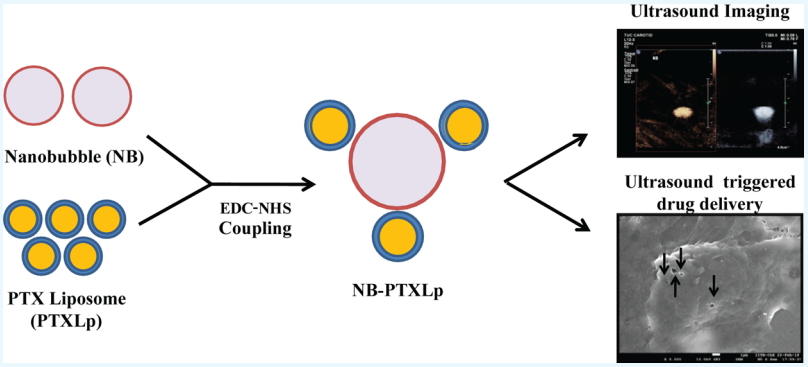

ABSTRACT: The ability of ultrasound contrast agents to enhance the cell membrane permeability in response to an ultrasound pulse has unveiled avenues to facilitate the delivery of a higher intracellular payload at target sites. In light of the above, we report the development of submicron-sized (528.7 ± 31.7 nm) nanobubble-paclitaxel liposome (NB-PTXLp) complexes for ultrasound imaging and ultrasound responsive drug delivery in cancer cells. With a paclitaxel entrapment efficiency of 85.4 ± 4.39%, the 200 nm-sized liposomes tethered efficiently (conjugation efficiency ∼98.7 ± 0.14%) with the nanobubbles to form conjugates. Sonoporation of MiaPaCa-2 cells upon treatment with nanobubbles and ultrasound enhanced cellular permeability, resulting in 2.5-fold higher uptake of liposomes in comparison to only liposome treatment. This manifested into more than 300-fold higher anticancer activity of NB-PTXLps in the presence of ultrasound in MiaPaCa-2, Panc-1, MDA-MB-231, and AW-8507 cell lines, compared to commercial formulation ABRAXANE. Also, the NB-PTXLp conjugates were found to exhibit echogenicity comparable to the commercial ultrasound contrast agent SonoVue. In addition, the developed nanobubbles were found to exhibit more than 1 week echogenic stability as opposed to 6 h stability of the commercially available ultrasound contrast agent SonoVue. Hence, the NB-PTXLps developed herein could prove to be a promising and minimally invasive theranostic platform for cancer treatments in the future.

1. INTRODUCTION

The basic prerequisite for an effective cancer therapy is an on-demand availability of the chemotherapeutic agent at the target site and a low to negligible level of systemic toxicity. The success of conventional cancer chemotherapy is limited by the nonspecificity and poor bioavailability of the chemotherapeutic drug, culminating in undesirable side effects.[1−6] A paradigm shift toward the usage of biocompatible and biomimetic nanocarriers for drug delivery over the past decades partially combated the above limitations by shielding the drug and decreasing the systemic toxicity.[7−11] Despite the availability of a broad range of nanocarriers, their poor pharmacokinetics fails to address the issue of site-specific bioavailability limiting their translation from bench to bedside.

The pursuit of precision medicine led to the exploration of triggers for on-site application that can be tuned to stimulate an on-demand release of therapeutic from the nanocarriers, enhancing site-specific bioavailability.[12−19] A broad range of triggers like heat, NIR radiation, magnetic waves, ultrasound (US), pH, and enzymes are currently being evaluated for development of trigger-responsive drug delivery systems (DDS).[20−24] Additionally, with an objective to enable clinicians to visualize the nanocarrier accumulation and therapeutic release at the target site, an array of imaging probes are currently being developed which can be incorporated into the trigger-responsive DDS.[25−29] The advancements in imaging technologies like optical imaging, X-ray, computed tomography, magnetic resonance, and US can leverage the potential of the image-guided DDS not only for drug delivery but also to monitor the post treatment changes at the site of application to assess the progress of the treatment regimen.

Received: June 27, 2019
Accepted: August 27, 2019
Published: September 12, 2019

DOI: 10.1021/acsomega.9b01924
ACS Omega 2019, 4, 15567−15580

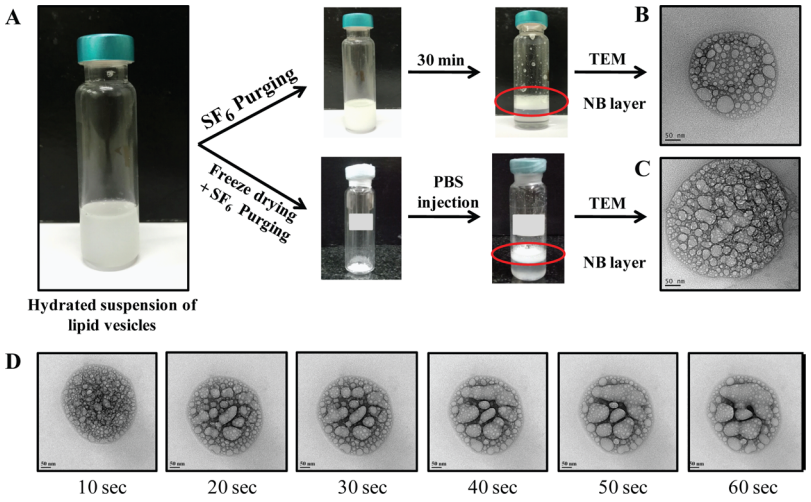

Figure 1. [A] NB preparation showing the formation of compact middle layer for both freshly prepared and reconstituted NBs. Transmission electron micrographs of [B] freshly prepared NBs and [C] reconstituted NBs (scale bar—50 nm) showing the presence of spherical gas pockets. [D] Time lapse imaging of NBs under 200 kV electron beam showing coalescence of gas pockets.

US imaging is the most common diagnostic imaging modality because it is safe, affordable, and noninvasive and there is no risk of ionizing radiation. However since the past few decades, US is also being explored for drug delivery applications in addition to imaging. The underlying basis of US therapy is US contrast agents (UCA) or microbubbles (MB) which are gas-filled spheres composed of lipid, polymer, protein, or their combination, ranging in size from 1 to 8 μm.[30,31] Upon US application, these MBs undergo a controlled contraction and expansion referred to as cavitation, reflecting the incident US waves that are captured by the transducer probe and converted to an image. Because the gas-filled MBs exhibit higher compressibility than biological tissues, they reflect US more effectively than the tissues. This enhances the contrast of the region of interest, a property well known as echo reflection or echo enhancement.[32] There have been consolidated efforts to stabilize MBs by the introduction of a stabilizing shell and plasma-insoluble gases (SF_6 and perfluorocarbons) to enhance their residence time in the body as well as enhance the US-reflecting ability.[33]

On the therapeutic front, the US-induced cavitation of MBs in the vicinity of biological cells was found to induce the formation of temporary sonopores, resulting in an enhanced permeability which could be exploited for site-specific US-responsive drug delivery.[34] Additionally, the MB cavitation was also found to have other biological effects like localized temperature increase, reactive oxygen species generation, and stimulation of receptor-mediated endocytosis.[35,36] Several studies have also reported the local extravasation of macromolecules and nanoparticles induced by MBs in response to US.[37] These developments inspired the use of physical mixture MBs and chemotherapy drugs for anticancer treatments. Commercial UCA formulation SonoVue was used in combination with gemcitabine HCL for the treatment of pancreatic ductal adenocarcinoma (PDAC).[38] With a view to reduce the systemic toxicity, drug-loaded MBs were developed; however, the low surface area-to-volume ratio attributed to the micron size of MBs limited their drug loading capacity.[39] This would require administering either a high dose of MBs or increasing the dosage frequency, consequently elevating costs. In an attempt to increase the therapeutic payload, the MBs were coated with drug-loaded nanocarriers to form pendant-shaped complexes.[40] However the limitation of such an approach was the micron size of the complexes that limited their extravasation to the tumor site, reducing the overall therapeutic efficacy. Therefore size reduction of MBs is currently the need of the hour because there have been studies reporting the uptake of MBs by the reticulo-endothelial system (RES) in a size-dependent manner.[41] A reduction in size of the above stated complexes would be beneficial not only for an unhindered passage through the capillary bed but also for efficient extravasation through the leaky vasculature of the tumor, enhancing their accumulation in the tumor interstitium via the enhanced permeability and retention effect.

With a view to address the limitations of the US-responsive DDS cited above, herein we report the development of submicron-sized nanobubble-paclitaxel liposome (NB-PTXLp) complexes as the theranostic platform for US imaging and drug delivery in cancer cells. We hypothesize that the US-induced cavitation of nanobubbles (NBs) would enhance the cancer cell permeability, increasing the uptake of drug-loaded liposomes (Lps). The subsequent enhancement of the intracellular therapeutic payload would manifest into higher anticancer activity.

2. RESULTS AND DISCUSSION

2.1. Characterization of NBs. NBs were prepared by the thin-film hydration method, wherein the lipid vesicles formed post hydration were subject to purging of SF_6 gas. The bubble layer was seen floating on the top of the tubes (Figure 1A). Vigorous mixing of the stabilized NBs restored the milky appearance to the entire suspension, which when allowed to stand reseparated into the top layer of NBs and bottom layer of clear and transparent phosphate-buffered saline (PBS), indicating the formation of a stable layer of NBs. Physicochemical characterization revealed hydrodynamic size, zeta potential, and polydispersity index (PDI) of the NBs to be 320 ± 30.2 nm, 9.3 ± 1.47 mV, and 0.261 ± 0.07, respectively. The hydrodynamic size of the NBs was found to be significantly lower as compared to the size of the UCAs reported in the literature.[39] A nanometer size range for UCAs is beneficial, as it can facilitate unhindered passage through the capillary bed and efficient extravasation into the tumor

DOI: 10.1021/acsomega.9b01924
ACS Omega 2019, 4, 15567−15580

Table 1. Summary of Hydrodynamic Size (nm), Zeta Potential (mV), and PDI of DPPC/DOPE (9:1) Liposome (Lp), PTX-Loaded Lps (PTXLp), NBs, Reconstituted NBs (Recon NBs), and NB-PTX Liposome Conjugates (NB-PTXLp)

	hydrodynamic size (nm)	zeta potential (mV)	PDI
Lp (DPPC/DOPE—9:1)	163.1 ± 10.65	−6.8 ± 4.1	0.18 ± 0.02
PTXLp (lipid/PTX—15:1)	190.1 ± 19.4	−6.5 ± 3.7	0.19 ± 0.04
NB	320 ± 30.2	9.3 ± 1.47	0.261 ± 0.07
recon NB	383 ± 41.6	8.7 ± 1.1	0.395 ± 0.1
NB-PTXLp	528.7 ± 31.7	−7.1 ± 2.5	0.55 ± 0.1

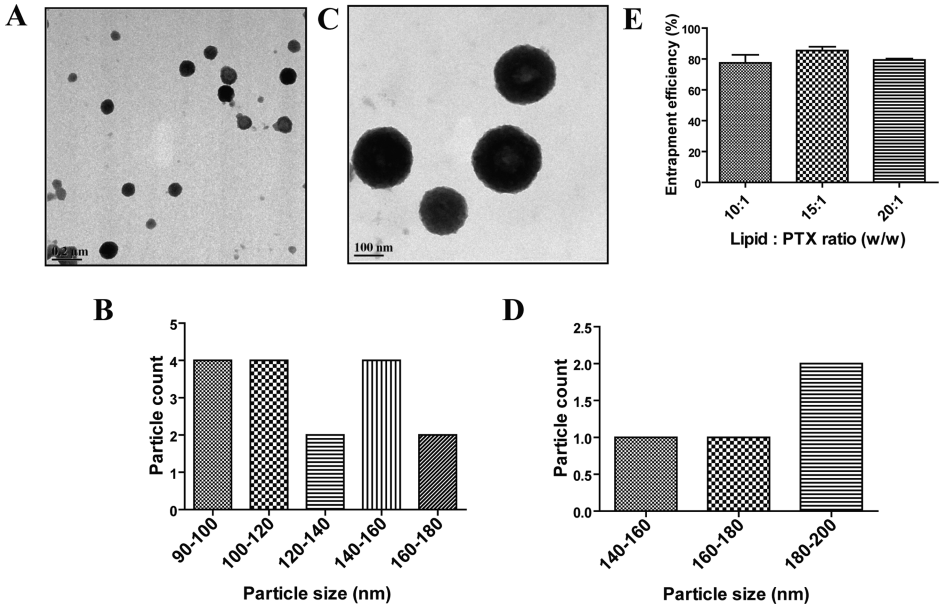

Figure 2. [A] Transmission electron micrograph of DPPC/DOPE (9:1) Lps (scale bar—200 nm). [B] DPPC/DOPE (9:1) liposome size distribution histogram from TEM micrograph [C] Transmission electron micrograph of PTX-loaded Lps with lipid/PTX ratio 15:1 (scale bar—100 nm). [D] PTX-loaded Lps size distribution histogram from TEM micrograph. [E] PTX entrapment efficiency for liposomal formulations with varying lipid/PTX ratios.

interstitium via the leaky vasculature, where the size of the tight junctions is typically between 100 and 780 nm.[42] Additionally, it can also confer a long circulating time to the NBs by escaping the size-dependant uptake by the RES. Zeta potential is a measure of the colloidal stability of the nanoparticulate formulation, wherein a higher magnitude is an indicative of interparticle repulsive forces that prevent particle aggregation. The NBs were found to have a positive charge on the surface as indicated by the zeta potential. PDI is a measure of the heterogeneity of the colloidal particulate system, where lower PDI values are desirable for a monodispersity of the particulate suspension. A PDI value of 0.261 ± 0.07 for NBs was found to be significantly lower as compared to that of the commercial UCA formulation SonoVue,[43] indicating a monodisperse suspension of NBs (Figure S1). Transmission electron micrographs revealed particles with a spherical architecture, and the size of the NBs was in agreement with the DLS size (Figure 1B). Interestingly, the transmission electron microscopy (TEM) micrographs also revealed the presence of characteristic pocket-shaped cavities which could be attributed to the gas pockets of SF_6. A time lapse imaging of the NBs under the 200 kV electron beam for 1 min revealed a dynamic coalescence of the pocket-shaped cavities, indicating the deflation of the NB architecture under the high-energy electron beam (Figure 1D).

Reconstituted NBs were prepared by injecting PBS into the sealed vial containing lyophilized vesicles in an SF_6-purged headspace. Following vigorous shaking for efficient redispersion, the vesicles were found to rise and form a compact mass of reconstituted NBs, similar to that of freshly prepared NBs. The hydrodynamic size, zeta potential, and PDI of the reconstituted NBs was found to be 383 ± 41.6 nm, 8.7 ± 1.1 mV, and 0.395 ± 0.1. The hydrodynamic size and PDI of the reconstituted NBs were found to be marginally higher than that of freshly prepared NBs, whereas the zeta potential was marginally lower; however, the difference was not statistically significant. This indicates that the reconstitution of the NBs does not significantly alter their physicochemical properties in comparison to the freshly prepared counterparts. This is essential for the long-term storage of the freeze-dried formulation that can be reconstituted just prior to usage. Additionally, the biocompatibility of the NBs was evaluated on murine fibroblast cell line (L929), wherein cell viability greater than 90% was observed for NB concentration as high as 100 μg/mL (Figure S2), rendering them suitable for further studies.

2.2. Characterization of Lps. 1,2-Dipalmitoyl-*sn*-glycero-3-phosphocholine (DPPC)/1,2-dioleoyl-*sn*-glycero-3-phosphoethanolamine (DOPE) (9:1) Lps were also prepared by the thin-film hydration method. Physicochemical characterization (Table 1) revealed the hydrodynamic size, zeta potential, and PDI to be 163.1 ± 10.65 nm, −6.8 ± 4.1 mV, and 0.18 ± 0.02, respectively. Moreover, transmission electron micrographs also showed a monodisperse population of

DOI: 10.1021/acsomega.9b01924
ACS Omega 2019, 4, 15567−15580

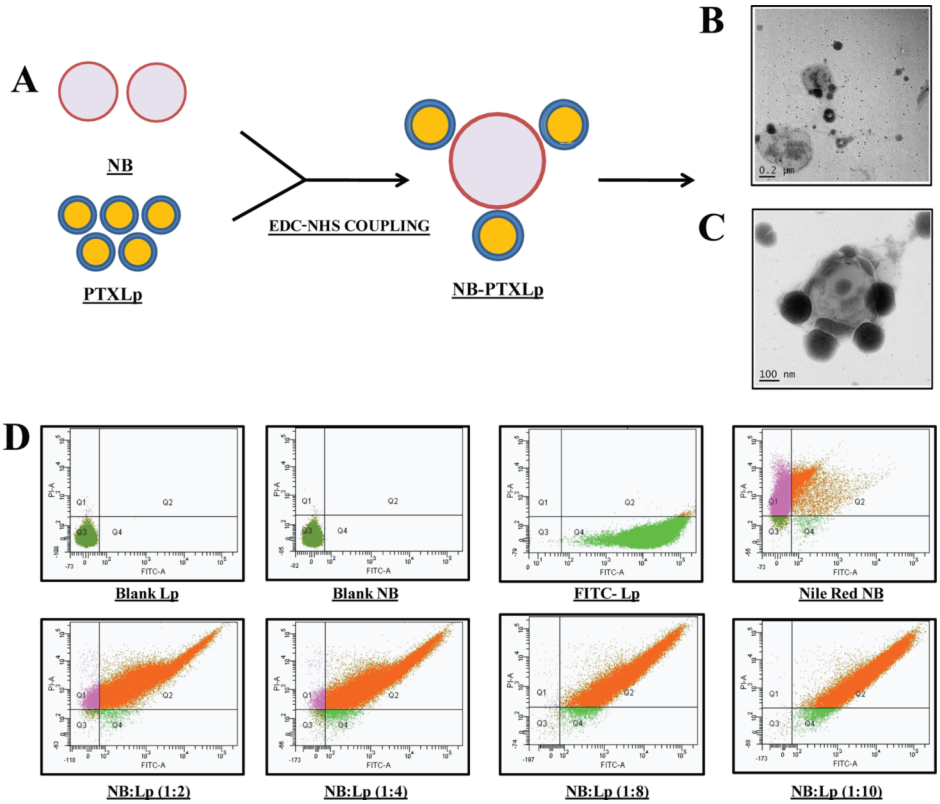

Figure 3. [A] Illustration depicting the formation of NB-PTXLp conjugates by EDC/NHS coupling, [B] Transmission electron micrograph of NB-PTXLp conjugate (scale bar—200 nm), [C] Transmission electron micrograph of NB/PTXLp conjugate (scale bar—100 nm), and [D] Evaluation of NB-Lp conjugation efficiency by FACS.

spherical particles with diameters lesser than 200 nm (Figure 2A), which was in agreement with the DLS data. The zeta potential of the Lp suspension indicated a negative surface charge, a factor that could enhance their coupling efficiency with the positively charged NBs via electrostatic interactions, in addition to covalent coupling. Additionally, the biocompatibility of the LPs was evaluated on murine fibroblast cell line (L929), wherein cell viability greater than 90% was observed for Lp concentration as high as 100 μg/mL (Figure S2), allowing safe usage for further studies.

2.3. PTX Entrapment and Drug Loading. Drug-loaded Lps were prepared by incorporation of paclitaxel (PTX), a potent microtubule stabilizing anticancer drug,[4445−47] into the hydrophobic shell of the Lps. Batches of Lps were prepared by varying the concentration of PTX (lipid/PTX ratios—10:1, 15:1, and 20:1), and the amount of PTX incorporated was quantified by high-pressure liquid chromatography (HPLC) (Figure 2E). The 10:1 batch was found to have PTX entrapment of 77.4 ± 9.15% with a drug loading of 4.29 ± 0.5%. However, a visible leaching of PTX was observed upon being allowed to stand for 15 min negating its use for further studies. Amongst the other two combinations, the 15:1 batch was found to have a higher entrapment efficiency and drug loading of 85.4 ± 4.39 and 4.98 ± 0.25%, respectively, and hence taken ahead for further developments. The hydrodynamic size, zeta potential, and PDI of the 15:1 PTX-loaded liposomal batch was found to be 190.1 ± 19.4 nm, −6.5 ± 3.7 mV, and 0.19 ± 0.04, respectively. Though a marginal increase in the hydrodynamic size was evident in comparison to the nondrug-loaded Lps, the difference was not statistically significant. Additionally, a monodisperse population with a spherical morphology and size ∼200 nm was observed in the transmission electron micrographs of the PTX-loaded Lps (Figure 2C).

2.4. Development of Nanobubble/Liposome Conjugates. The NBs and Lps were conjugated via 1-ethyl-3-(3-dimethylaminopropyl) carbodiimide hydrochloride (EDC)/*N*-hydroxy succinimide (NHS) coupling by leveraging the 1° amine group of DOPE in liposome and carboxylate group of stearic acid in NBs toward the formation of an amide linkage. Fluorescein isothiocynate (FITC)-labeled Lps and Nile red-loaded NBs were subject to conjugation using different NB/Lp ratios (1:2, 1:4, 1:8, and 1:10), and the conjugation efficiency was evaluated by flow cytometry analysis (Figure 3D). Quantification of the double fluorescent population revealed an increasing trend in conjugation efficiency from 91.5 ± 0.23% in 1:2 batch to 98.7 ± 0.14% in 1:10 batch. Though a high degree of conjugation efficiency (>90%) was observed for all the four batches, the difference was not statistically significant. However, in order to develop a formulation with the maximum PTX loading, the 1:10 (NB/Lp) batch was chosen for further studies. The hydrodynamic size, zeta potential, and PDI of the nanobubble-PTXliposome conjugates (NB-PTXLp) were found to be 528.7 ± 31.7 nm, −7.1 ± 2.5 mV, and 0.55 ± 0.1, respectively. An expected increase in the size of the conjugates was observed to be attributed to the tethering of Lps on the surface of NB's. Transmission electron micrograph showed 200 nm size PTX Lps latched onto the surface of NB (Figure 3C), providing a visual proof toward the formation of NB-PTXLp conjugates. The heterogeneity of the conjugate system was also found to have increased in comparison to the NBs and Lps as indicated by the PDI

DOI: 10.1021/acsomega.9b01924
ACS Omega 2019, 4, 15567−15580

values. Development of the NB-PTXLp conjugates with a size ∼500 nm is an important benchmark in comparison to the micron size conjugates. The submicron size would not only enable unhindered passage through the capillary bed but also facilitate efficient extravasation from the leaky tumor vasculature (tight junctions: 100−780 nm) into the tumor interstitium. Moreover a submicron size of NB-PTXLp would also facilitate their better proximity to the cancer cells enhancing the effects of cavitation which are distance dependent, to induce a cell membrane permeability and subsequent increase in the intracellular therapeutic delivery.

2.5. In Vitro PTX Release. PTX being a hydrophobic drug has been known to exhibit slow and sustained release from nanocarriers. From the release profile (Figure 4), it is evident

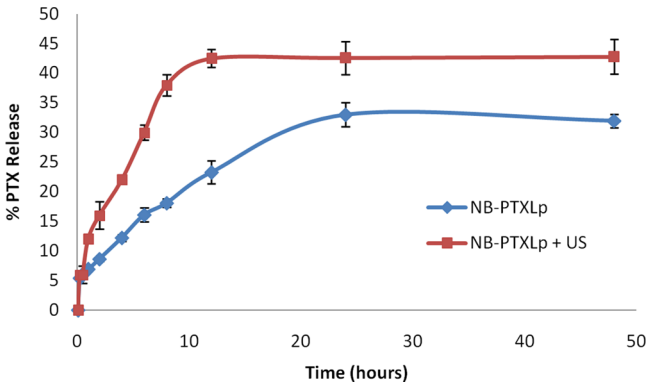

Figure 4. In vitro release profile of PTX from NB-PTXLp conjugates in the presence and absence of US at 37 °C.

that in the absence of an US pulse, a sustained release of PTX from the NB-PTXLp was observed up to 24 h, with ∼33% of the total entrapped PTX released at the end of 48 h. However, in the US-treated group, a burst release of PTX was observed within the first 8 h, consequently releasing ∼42% of the total entrapped PTX at the end of 48 h which was 1.3-fold higher that the non-US-treated group. The results indicate the beneficial role of the applied US trigger in enhancing the release of PTX from the NB-PTXLp conjugates.

2.6. In Vitro Echogenicity. Echogenicity of the formulations was evaluated in a tissue mimicking phantom composed of 1% agarose gel[48] with embedded cylindrical wells for sample loading (Figure 5A). Post sample loading, the echogenic response was recorded in B-mode and contrast enhancement (CE) mode in the Philips EPIQ-7G US assembly by scanning the 12−3 MHz probe on the anterior surface of the agarose phantom. B-mode displays a signal for any material/region capable of reflecting US. However, a CE mode signal is a specific indication of harmonic signals, wherein the US frequency reflected by the UCAs is an integral multiple of the incident US frequency. No signal was obtained for the blank (PBS) and PTXLps because of their inability to reflect the US waves. However, a strong signal was obtained for NB, NB-PTXLps in both B and CE mode and was found to be equivalent to the signal obtained for the commercial UCA SonoVue (positive control) (Figure 5C). Interestingly, the reconstituted NBs exhibited a 1.25-fold stronger signal in comparison to SonoVue which was found to be statistically significant ($p < 0.05$) (Figure 5D). The strong signal in the CE mode was indicative of the harmonic cavitation exhibited by NBs, NB-PTXLps and reconstituted NBs. The comparable signal exhibited by NBs and NB-PTXLps is an indication that tethering Lps onto the surface of NBs does not compromise the imaging potential on NBs in the conjugate. Hence, a preliminary echogenicity evaluation confirmed the strong echogenic potential of NBs, NB-PTXLps, and reconstituted NBs.

To get finer insights into the stability and cavitation behavior of NBs and NB-PTXLps, a continuous echogenic response was evaluated over a time span of 10 min (Figure 6). It was observed that the NBs exhibited a strong and unaltered signal in the B-mode over the 10 min span; however, the CE mode showed a strong signal up to the 6 min mark, beyond which the signal was found to decrease gradually. Loss of the signal in the CE mode could be attributed to the gradual lipid shedding from the NB surface and subsequent leakage of SF_6 under

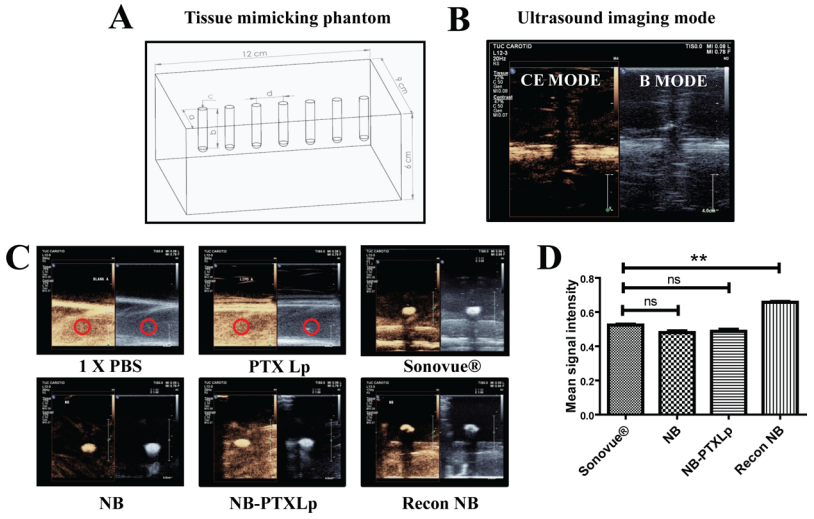

Figure 5. [A] Illustration of tissue mimicking 1% agarose phantom with embedded wells (a = 3 cm, b = 3 cm, c = 0.5 cm, d = 1.5 cm). [B] Representative image of B mode and CE mode, [C] Echogenic signal evaluation of 1× PBS pH 7.4 (−ve control), PTXLp (−ve control), SonoVue (+ve control), NB, NB-PTXLp, and reconstituted NB, and [D] Intensity analysis of CE mode signal exhibited by SonoVue (+ve control), NB, NB-PTXLp, and reconstituted NB (ns—not significant, $^{**}p < 0.01$).

DOI: 10.1021/acsomega.9b01924
ACS Omega 2019, 4, 15567−15580

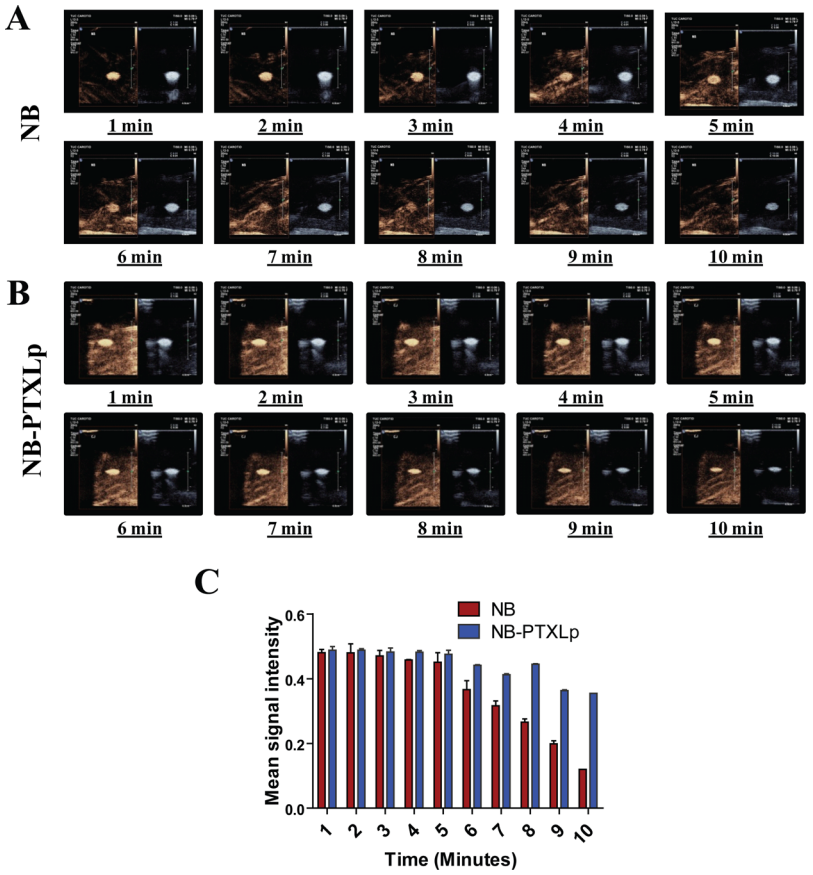

Figure 6. Time point echogenicity evaluation for [A] NBs and [B] NB-PTXLp. [C] Intensity analysis of CE mode signal exhibited by NBs and NB-PTXLp.

constant insonation that compromises on their ability to reflect the harmonic signals. On the other side, retention of a strong signal in B-mode up to 10 min indicated that though the NBs were stable and capable of reflecting US till the 10 min mark, their ability to reflect harmonics was gradually weakened beyond the 6 min mark. A similar time point evaluation of NB-PTXLps revealed a strong signal up to 10 min not only in the B-mode but also in the CE mode, which was in contrast to the CE mode signal exhibited by NBs. This confirmed the results obtained in the preliminary evaluation, where we observed that tethering Lps onto the surface of NBs does not compromise their imaging potential. Additionally, it is also an indication that decorating the bubbles with Lps could have limited the lipid shedding of the NBs, thus restricting gas leakage and allowing retention of strong signal in the CE mode up to the 10 min mark. Hence, liposome conjugation was observed to be a beneficial feature for enhancing the imaging potential of NB-PTXLps, adding to its theranostic potential.

In order to have a head-to-head comparison with the existing commercial US contrast agent, the echogenic response of reconstituted NBs and SonoVue was also evaluated over a 10 min time span (Figure 7). A strong and relatively unchanged signal was observed in B-mode and CE-mode for over the span of 10 min for both the samples. The reconstituted NBs were found to exhibit a stronger signal in the CE mode at all time points in comparison to SonoVue. Even at the 10th minute time point, the reconstituted NBs exhibited a 1.5-fold stronger signal than SonoVue which was found to be statistically significant ($p < 0.001$). This improvement in signal strength would help significantly in improving the sensitivity of contrast imaging used for current clinical applications. Additionally the presence of a −COOH group on the NBs could also be explored for attachment of ligands or biologicals toward the development of targeted NBs for varying disease pathologies. Hence, a strong imaging potential together with the targeting capability would be a stepping stone toward the development of promising prognostic systems for cancer, which is currently an unmet clinical need.

Development of theranostic platforms for cancer has always remained a challenge owing to the range of parameters that need to be addressed while fabricating such platforms. The two predominant challenges amongst many are the tumor location and the tumor microenvironment. As a well-established fact, the presence of tumors in the body can vary from the surface location like in breast cancer to deep-seated presence like PDAC. Additionally, because of accumulation of multiple mutations over several generations, the dedifferentiated tumor cells are heavily dependent on glycolysis that renders the tumor microenvironment acidic (~pH 6.5) in most of the cancers. Hence, in terms of the imaging potential, it is necessary for the NBs and NB-PTXLps not only to access and allow imaging of tumors at different locations but also to retain the imaging capability in the acidic tumor microenvironment. The pH response of NBs and NB-PTXLps was evaluated by suspending them in phosphate-buffered saline of pH 5.5 and 6.5. NBs and NB-PTXLps were found to exhibit a strong and comparable echogenic response at pH 6.5 prompting towards their ability to exhibit echogenic signals in the acidic microenvironment of the tumors (Figure 8A). Further, they were also found to display a strong and comparable response at

DOI: 10.1021/acsomega.9b01924
ACS Omega 2019, 4, 15567−15580

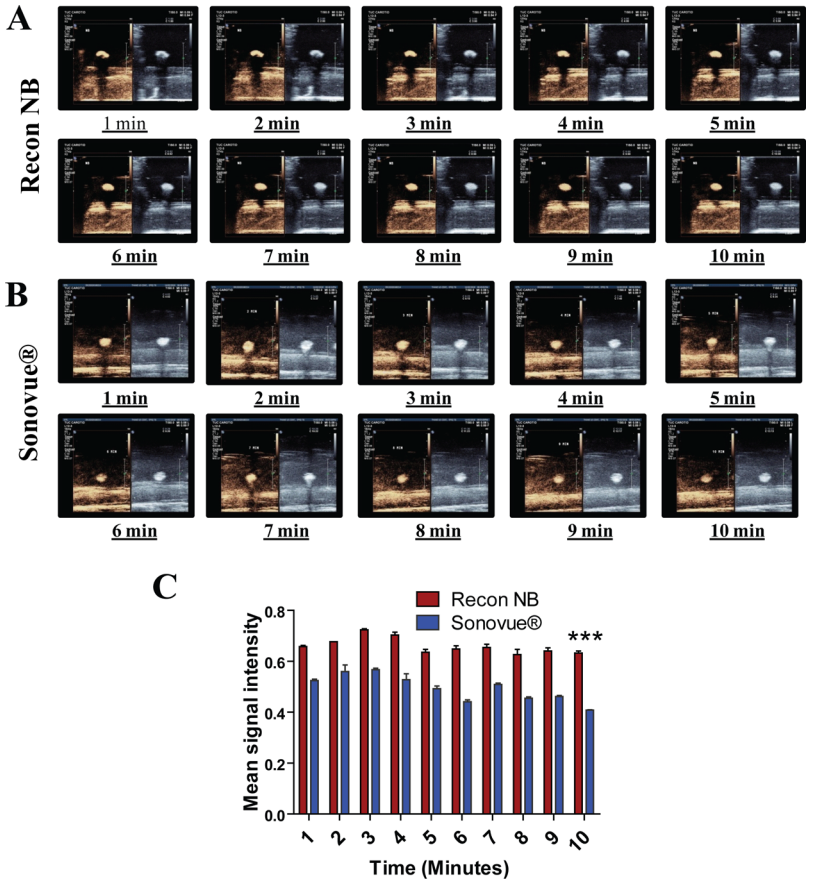

Figure 7. Time point echogenicity evaluation for [A] Reconstituted NBs and [B] SonoVue [C] Intensity analysis of CE mode signal exhibited by reconstituted NBs and SonoVue (***$p < 0.001$).

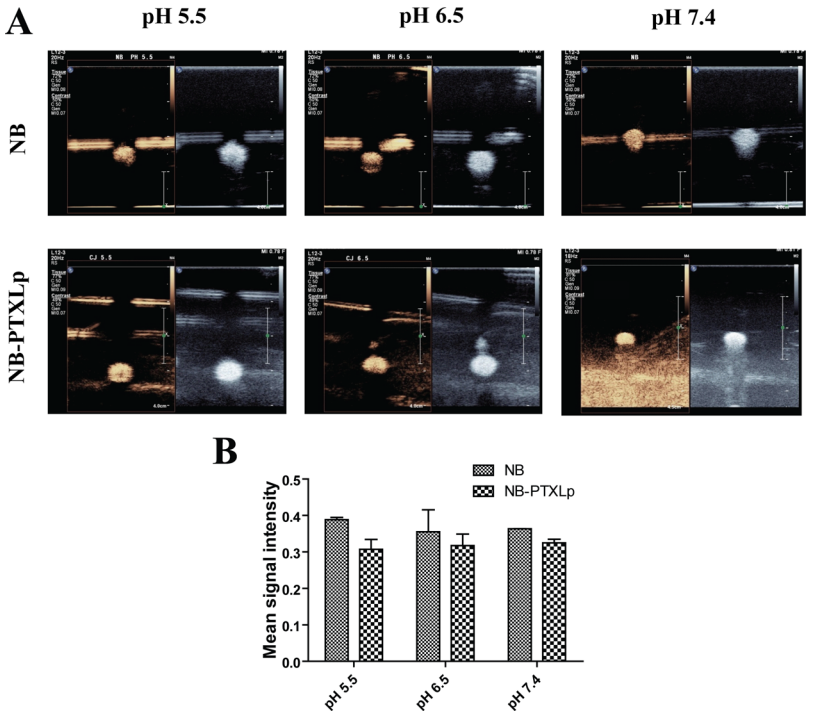

Figure 8. [A] Echogenicity evaluation of NBs and NB-PTXLp at pH 5.5, 6.5, and 7.4. [B] Intensity analysis of CE mode contrast exhibited by NB and NB-PTXLp at variable pH.

pH 5.5. An acidic pH of 5.5 is generally encountered in the endosomal compartment of the cell. Though the study is not aimed at addressing endosome related features, however if it were to address them for future applications, the strong

DOI: 10.1021/acsomega.9b01924
ACS Omega 2019, 4, 15567−15580

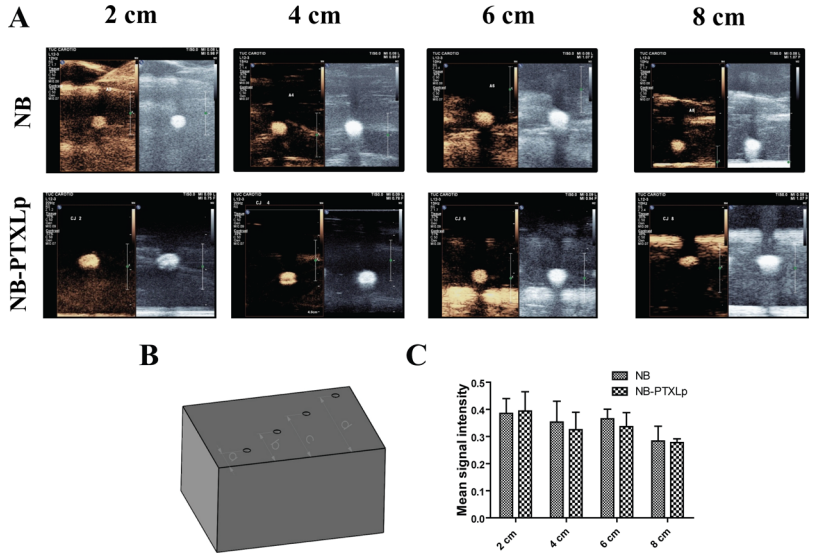

Figure 9. [A] Echogenicity evaluation of NBs and NB-PTXLp at a depth of 2, 4, 6, and 8 cm. [B] Modified tissue mimicking phantom of 1% agarose with wells embedded at different distances from the scanning surface corresponding to variable depths (a = 2 cm, b = 4 cm, c = 6 cm, d = 8 cm). [C] Intensity analysis of CE mode contrast exhibited by NB and NB-PTXLp at variable depths.

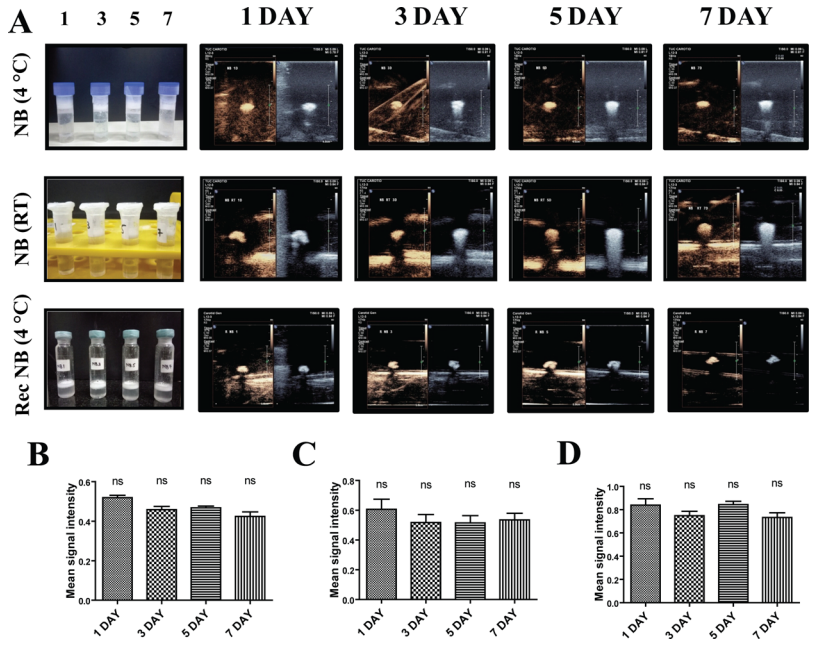

Figure 10. [A] 1−7 day echogenic response of NBs stored at 4 °C and RT, reconstituted NBs stored at 4 °C. Stable middle layer of NB observed at 4 °C and RT and reconstituted NB at 4 °C. Intensity analysis of CE mode contrast exhibited by [B] NB at 4 °C [C] NB at RT and [D] Reconstituted NB at 4 °C (ns—not significant).

echogenic response of NBs at pH 5.5 would be an added benefit for US imaging. In addition, in-depth response of NBs and NB-PTXLps was evaluated using a modified tissue-mimicking phantom (Figure 9B) with sample wells embedded at different depths (2, 4, 6, 8 cm) from the imaging surface. Strong echogenic signals were observed for NBs and NB-PTXLps in both B mode and CE mode at all the four depths studied (Figure 9A), and the variation in the signal strength over multiple depths was not statistically significant. Hence, the study proved the potential of NBs and NB-PTXLps to exhibit not only a strong imaging signal at multiple depths but also their stability and imaging capability post dispersion in the acidic tumor microenvironment.

2.7. Storage Stability of NBs. To determine the storage conditions for maximum stability, the prepared NBs were subjected to preliminary stability testing at 4 °C and room temperature over a span of 1 week. Stability end points were retention and compactness of the NB middle layer and subsequent echogenic response evaluation. Physical observations revealed that under both the conditions of storage, the layer of NBs was found to be compact and undisturbed over the 7 day period (Figure 10A). The echogenic response evaluation revealed strong intensity in B-mode and CE mode from day 1 to day 7 for NBs stored at both 4 °C and room temperature. The difference between day 1 and day 7 signal intensity was not statistically significant. For comparison with

DOI: 10.1021/acsomega.9b01924
ACS Omega 2019, 4, 15567−15580

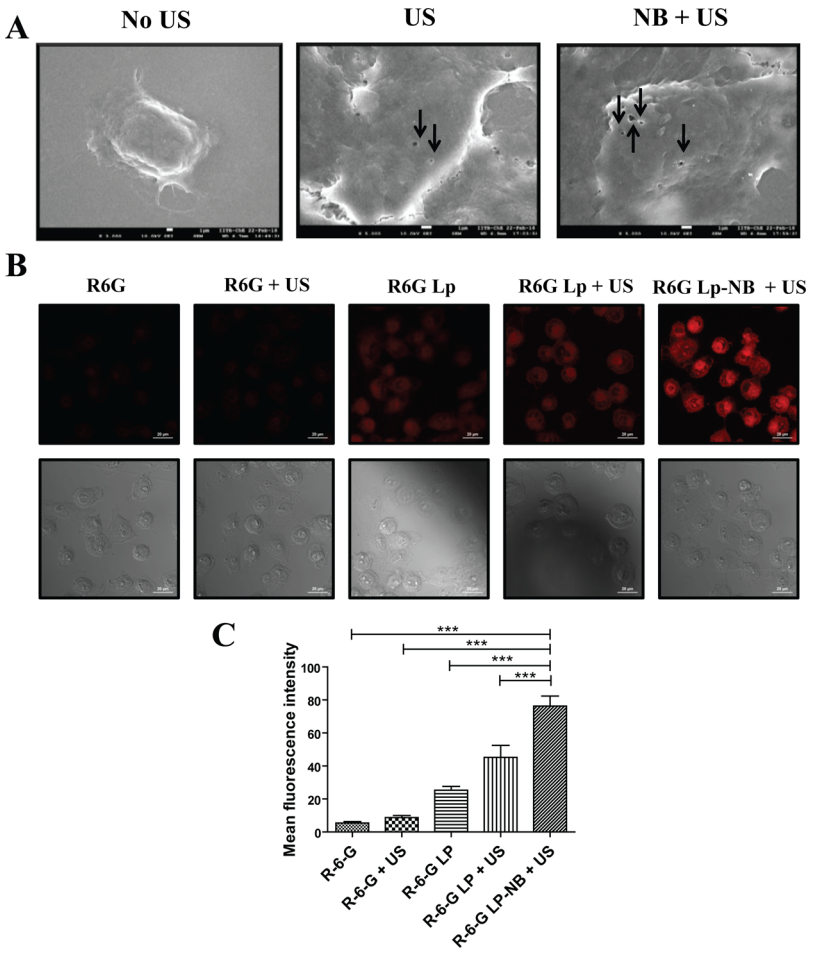

Figure 11. [A] Scanning electron micrograph of MiaPaca-2 cells untreated, US treated, and NB + US treated (scale bar—1 μm). Arrows indicate the sonopore formation on the cell membrane of MiaPaca-2 cells. [B] Confocal laser scanning microscope images (fluorescence and differential interference contrast) of MiaPaca-2 cells treated with R6G, R6G + US, R6G Lp, R6G-Lp + US, and NB-R6G-Lp + US. (scale bar—20 μm). [C] Fluorescence intensity analysis of MiaPaca-2 cells treated with R6G, R6G + US, R6G Lp, R6G-Lp + US, and NB-R6G-Lp + US (***$p < 0.001$).

the commercial agent SonoVue which has a stability of 6 h post reconstitution,[43] we evaluated the storage stability of reconstituted NBs at 4 °C over a 1 week span. Strong echo intensity was observed from day 1 to day 7, with the difference not being statistically significant (Figure 10A). This evidently prompted to a minimum 1 week stability of reconstituted NBs, which was significantly higher in comparison to the 6 h stability of SonoVue post reconstitution. In addition to the storage stability, we also determined the minimum concentration of NBs that could give a strong echogenic response for efficient clinical imaging. The NBs were subjected to a dilution from 5000 to 1 μg/mL followed by echogenicity evaluation (Figure S3). Strong echogenic signal was obtained for concentrations up to 5 μg/mL, followed by a 4-fold reduction in signal intensity for 1 μg/mL, indicating that an NB concentration as low as 5 μg/mL could be used for clinical imaging.

2.8. US-Triggered Cellular Sonoporation. In order to determine the effect of US on cellular morphology, a preliminary evaluation was conducted on L929 murine fibroblast cells. An US pulse of 1 W/cm^2 and 75% duty cycle was applied to a monolayer of adhered L929 cells for 30 s. In group 1, the cells were formaldehyde fixed immediately post pulsing whereas in group 2, a recovery time of 4 h was allowed post US pulsing and followed by fixing the cells. Both the treatment groups were then observed under cryo-FEG-SEM (Figure S5). A total of 100 cells were imaged for both the groups. In group 1, 87/100 cells exhibited membrane disruptions on the surface known as sonopores. However, in group 2, only 4/100 cells were found to have the sonopores, indicating transient existence of sonopores that reseal with time. US induces cavitation of dissolved gas pockets on the surface of the cells which causes a directional fluid displacement on the surface of the cells referred to the microjets. As a consequence of microjetting, a shear force is exerted on the cell surface that results in localized disruption of the membrane leading to the formation of sonopores. These sonopores eventually act a physical passage for broad range of micro/macromolecules in the vicinity of the pore to gain entry into the cellular cytosol. To evaluate the role of NBs in sonopore formation, a similar experiment was carried out with PDAC cell line MiaPaCa-2 (Figure 11A). In the group treated with only US (1 W/cm^2, 75% duty cycle, 30 s), 85/100 cells scanned were found to exhibit the presence of sonopores having an average size of ∼400 nm, and the average number of pores per cell was found to be ∼2. However, in the NB + US group, 96/100 cells were found to show the presence of sonopores having an average size ∼550 nm and average number of pores per cell was ∼4 (Table 2). Hence, it was evident that treatment with NBs in the presence of US not

DOI: 10.1021/acsomega.9b01924
ACS Omega 2019, 4, 15567−15580

Table 2. Quantification of Sonopore Positive Cells, Average Sonopore Size, and Sonopore Count/Cell in MiaPaCa-2 Cell Line Post Application of US and NBs + US (NB + US)

	no US	US	NB + US
cells counted	100	100(85)	100(96)
avg pore size (nm)		403.7 ± 68.3	552.8 ± 164.3
avg pore count/cell		~2	~4

only increased the pore size but also increased the number of pores per cell. This overall enhancement in the extent of sonoporation is attributed to the US-induced cavitation of NBs, which significantly enhances the cell membrane permeability.

2.9. US-Triggered Cellular Uptake. The effect of NBs and US on cellular uptake of external cargo was observed in MiaPaca-2 cell line. On a general note, US-treated groups (1 W/cm^2, 75% duty cycle, 30 s) were found to have higher uptake of free R-6G and R-6G-loaded Lps in comparison to the non-US-treated groups. The R-6G-Lp + US and the NB-R6g-Lp + US group showed a 1.5- and 2.5-fold higher uptake of Lps, respectively, in comparison to the non-US-treated R-6G-Lp group (Figure 11B). Higher fluorescence signal observed in conjugate treatment could be attributed to the close proximity of Lps to the NBs, resulting in higher uptake upon US application. Hence, the cumulative analysis of sonoporation and internalization data present a concrete evidence that US enhances the cell membrane permeability by the formation of transient sonopores on the surface of the cell, allowing a higher uptake of extracellular cargo. However in the presence of NBs, the permeabilization effect is further enhanced by increasing the number and size of sonopores, a property which can be efficiently leveraged for an efficient and tunable US-triggered intracellular drug delivery.

2.10. In Vitro Cellular Cytotoxicity. The anticancer effect of PTX, PTXLp, NB-PTXLp, and NB-PTXLp + US was evaluated on MiPaCa-2, Panc-1, MDA-MB-231, and AW-8507 cell lines. Commercial paclitaxel containing formulations ABRAXANE and PACLITAX were used as positive controls. An increase in cytotoxicity (in terms of lowered IC_{50}) was observed when the PTX was incorporated into Lps as compared to equivalent amount of free PTX (Table S1). This highlights the beneficial role of biomimetic nanocarriers like Lps in enhancing the therapeutic bioavailability by enveloping the drug moieties. Further, a several fold decrease in IC_{50} was observed for the NB-PTXLp + US group as compared to all other groups in the four cell lines (Figure 12). NB-PTXLp + US was found to have almost 1000-fold higher cytotoxicity in comparison to free PTX in MiaPaca-2, Panc-1, and MDA-MB-231 and 100-fold higher toxicity in AW-8507 cell line. Furthermore the NB-PTXLp + US also exhibited a 10-fold and 100-fold reduction in IC_{50} in comparison to PTX liposome for Miapaca and Panc-1 cell line, respectively. Also, in all of the four cell lines, NB-PTXLp + US exhibited several fold higher cytotoxicity in comparison to the commercial PTX formulations ABRAXANE and PACLITAX. The result highlights the overall improvement in the anticancer activity upon drug incorporation into a biocompatible liposomal nanocarrier which is further enhanced upon application of an external trigger like US. Reduction in IC_{50} not only helps to lower the overall dosage of the drug thereby enhancing the therapeutic efficacy of the formulation but also reduces the systemic side effects and improves the patient compliance. However,

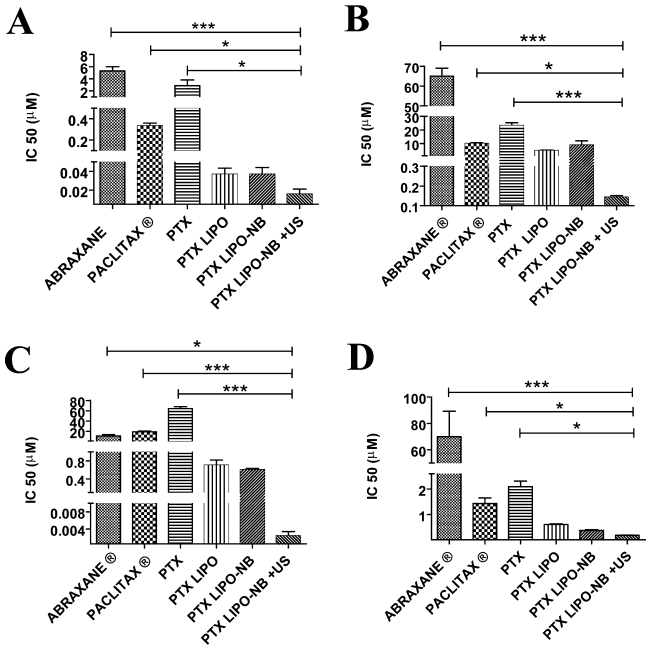

Figure 12. In vitro cytotoxicity of NB-PTXLp + US in [A] MiaPaCa-2 cell line, [B] Panc-1 cell line, [C] MDA-MB-231 cell line, and [D] AW-8507 cell line in comparison to ABRAXANE, PACLITAX, PTX, PTXLp, and NB-PTXLp in the absence of US (*p < 0.05, ***p < 0.001).

validation of the formulation in preclinical models is an essential feature prior to clinical usage.

3. CONCLUSIONS

Summarizing the above work, submicron-sized (~500 nm) nanobubble-paclitaxel liposome complexes (NB-PTXLp) were successfully prepared for US contrast imaging and US-triggered drug delivery in cancer cells. Binding of Lps on the surface of NBs did not compromise the imaging potential of the NB-PTXLp theranostic system. Moreover, the US induced cavitation of NBs resulted in the sonoporation of cancer cells enhancing their permeability. This facilitated enhanced cellular uptake of PTX-loaded Lps, resulting in several fold higher anticancer efficacy of NB-PTXLps compared to the commercial formulations ABRAXANE and PACLITAX, confirming our hypothesis. Although promising as a theranostic platform for in vitro evaluation, a comprehensive preclinical study needs to be undertaken to realize the theranostic potential of NB-PTXLps for clinical applications.

4. MATERIALS AND METHODS

4.1. Materials. DPPC (99%) and DOPE (99%) were purchased from Avanti Polar Lipids Inc (Alabaster, USA). Paclitaxel (99%) was obtained as a gift sample from Mac-Chem Products. Stearic acid (>98%) was purchased from Loba Chemie, EDC (99%), and dialysis membrane-50 was purchased from HIMEDIA, NHS (>97%) was purchased from Sisco Research Lab, and rhodamine-6G (>97%), Nile red (>98%), and FITC (>90%) were purchased from Sigma-Aldrich and agarose from MP Biomedicals. HPLC grade methanol and chloroform were purchased from Merck, Mumbai (India). Human PDAC cell lines MiaPaCa-2 and Panc-1, triple negative human breast cancer cell line MDA-MB-231, and head and neck cancer cell line AW-8507 were

DOI: 10.1021/acsomega.9b01924
ACS Omega 2019, 4, 15567−15580

procured from National Centre for Cell Sciences, (NCCS) Pune. Dulbecco's modified Eagle medium (DMEM), Dulbecco's phosphate buffered saline 1×, Trypsin EDTA solution, and fetal bovine serum were purchased from HIMEDIA. Degassed water was used in the preparation of tissue mimicking agarose phantoms for US echogenicity studies.

4.2. Preparation of NBs. The NBs were prepared by thin-film hydration method described as follows: Briefly, DPPC and stearic acid were weighed in a molar ratio of 9:1, and a thin film was prepared in a round-bottom flask using a chloroform/methanol solvent mixture (2:1 by volume). The thin film was hydrated with PBS 1× pH 7.4 at 180 rpm and 45 °C in a rotary evaporator for 1 h, to achieve a final concentration of 2 mg/mL. Post hydration, the suspension was purged with SF_6 gas and subsequently allowed to stand in a tube for 30 min to allow the formation of NBs. The hydrodynamic size of the NBs was determined by dynamic light scattering (DLS). Surface charge/zeta potential was determined using Brookhaven ZetaPALS. Additionally, the structural features of the NBs were visualized by electron microscopy on a JEOL field emission gun—transmission electron microscope (Feg-TEM). For a comparative study with the commercial microbubble formulation, SonoVue, NBs were prepared as stated above with 1% D-mannitol as a cryoprotectant to achieve a final lipid concentration of 5 mg/mL in accordance with manufacturer instructions for SonoVue, followed by freezing at −196 °C in liquid nitrogen and subsequent freeze-drying in a lyophilizer for 48 h. The freeze-dried powder was transferred to a glass vial and sealed followed by purging of the headspace with SF_6 gas. Prior to usage, the vial was injected with 5 mL PBS 1× pH 7.4 and shaken vigorously for 60 s to obtain a uniform suspension of reconstituted NBs.

4.3. Preparation of Lps. The Lps were prepared by the thin-film hydration method described as follows: Briefly, DPPC and DOPE were weighed in a molar ratios 9:1 to form a thin film using chloroform/methanol mixture (2:1 by volume) in a round-bottom flask. The thin film was hydrated with PBS 1× pH 7.4 at 180 rpm and 45 °C on a rotary evaporator for 1 h. The hydrated suspension was subjected to sonication using a probe sonicator at a frequency of 20 KHz and 40% amplitude for 3 cycles of 2 min each at an interval of 1 min. The sonicated suspension was centrifuged at 15 000*g*, 4 °C for 30 min, and the pellet was reconstituted in PBS pH 7.4 to achieve a final concentration of 2 mg/mL. Paclitaxel-loaded Lps were prepared in a similar manner using three different lipid/drug ratios (10:1, 15:1, and 20:1), wherein PTX was added to the phospholipids mixture during the preparation of the thin film. The hydrodynamic size of the Lps was determined by DLS. Surface charge/zeta potential was determined using Brookhaven ZetaPALS. The structural features of Lps were visualized by electron microscopy on a JEOL Feg-TEM.

4.4. Evaluation of PTX Entrapment in Lps. Reverse-phase HPLC was used for quantification of PTX. The C18 reverse-phase HPLC column (LiChrosphere) was used as the stationary phase. Acetonitrile/Milli-Q (60:40 ratio) was used as the mobile phase with a flow rate of 1 mL/min and total runtime of 10 min. Standard curve of PTX was prepared in the range 5−15 μg/mL by dissolving the drug in methanol and preparing the further dilutions in the mobile-phase mixture. After the preparation of PTX Lps, the pellet obtained post centrifugation was resuspended in the PBS/methanol mixture (3:7 v/v) and subjected to the HPLC analysis. Post HPLC analysis, the % entrapment efficiency of PTX was determined with the following equation.

$$\% \text{ entrapment} = [C_p/C_0] \times 100$$

where C_p—concentration of PTX in the pellet and C_0—concentration of PTX in the hydrated-unsonicated formulation

4.5. Preparation of Nanobubble/Liposome Conjugates. NBs and Lps were prepared as described in Sections 4.2 and 4.3, respectively, and conjugated using the EDC/NHS coupling. Briefly, NBs were treated with 0.07% EDC and 0.04% NHS followed by addition of Lps and gentle mixing. The NB/Lp conjugation efficiency was determined by flow cytometry analysis. Lps were labeled with 0.1 mg/mL FITC, and NBs were labeled with 0.1 mg/mL Nile red. Conjugates were prepared as mentioned previously with NB/Lp ratios 1:2, 1:4, 1:8, and 1:10. Unlabeled NBs and Lps were used as negative controls. The percentage of double fluorescence positive population was recorded as a measure of the conjugation efficiency.

4.6. In Vitro PTX Release. In order to study the release kinetics of PTX upon application of US trigger, NBPTXLp's (group 1 and 2) were added to a dialysis membrane with a size exclusion limit of 50 kDa. A PBS/methanol (70:30 v/v) mixture was used as a sink to solubilize the released PTX. The sample-loaded membrane capsule was suspended in a 20 mL sink comprising of PBS/methanol (70:30 v/v) mixture in a 50 mL falcon tube. Group 2 was treated with an US pulse of 1 W/cm^2 and 75% duty cycle for 30 s, whereas group 1 served as the non-US-treated control. The tubes were then incubated at 37 °C in a shaker water bath at 60 rpm. One milliliter aliquots of the sink were withdrawn at regular time intervals up to 48 h, with simultaneous replenishment with 1 mL of fresh PBS/methanol (70:30 v/v) mixture. The amount of PTX released within the span of 48 h was quantified using HPLC as described in Section 4.4.

4.7. In Vitro Echogenicity Evaluation. NBs, PTXLps, and NB-PTXLp conjugates were prepared as described Sections 4.2, 2.3, and 2.5, respectively, with a concentration of 5 mg/mL. For echogenicity evaluation, a tissue mimicking phantom of 1% agarose was prepared with incorporated cylindrical wells for loading samples. After loading samples into the phantom wells, a 12−3 MHz probe was scanned on the anterior wall of the phantom, and the signal was observed using Philips EPIQ-7G US assembly in B-mode and CE mode. Degassed 1× PBS and PTXLps were used as negative controls and commercial contrast agent SonoVue was used as the positive control. Time point echogenic stability of the NBs, NB-PTXLp conjugates, and reconstituted NBs was evaluated by monitoring the echogenic signal over a span of 10 min under a constant US pulse. In order to determine the sensitivity of imaging response, NBs were subjected to dilution to achieve a concentration range from 5000 to 1 μg/mL and subjected to echogenic evaluation. To evaluate the echogenic response of NBs and NB-PTXLp conjugates at multiple depths, 1% agarose phantom was prepared with wells casted at multiple distances (2, 4, 6, 8 cm) from the scanning surface. pH stability of the NBs and NB-PTXLp conjugates was determined by suspending them in 1× PBS pH 5.5 and 6.5 then determining the echogenic response.

4.8. Storage Stability of NBs. To determine the storage stability at different temperatures, NBs were prepared as mentioned earlier with a final lipid concentration of 5 mg/mL and stored at 4 °C and room temperature, and echogenic

DOI: 10.1021/acsomega.9b01924
ACS Omega 2019, 4, 15567−15580

response of the stored NBs was recorded after 1, 3, 5, and 7 days using the agarose phantom assembly as described in Section 4.7.

4.9. Cell Culture. L929 murine fibroblast cell line, Human PDAC cell lines (MiaPaCa-2 and Panc-1), triple negative human breast cancer cell line (MDA-MB-231), and Human Head and Neck cancer cell line (AW-8507) were purchased from NCCS, Pune. The cell lines were maintained in DMEM containing 10% FBS (20% FBS for AW-8507) and 1% antibiotic−antimycotic solution under incubation conditions of 37 °C and 5% CO_2 in an atmosphere of 70% relative humidity.

4.10. US Triggered Cellular Sonoporation. MiaPaCa-2 cells were seeded at a density of 10^5 cells/well on a coverslip in a 24-well plate and incubated for 24 h at 37 °C in 5% CO_2 atmosphere and 70% relative humidity. Post incubation, spent media was discarded and replaced with freshly prepared NBs diluted to 10 μg/mL in DMEM. US pulse of 1 W/cm^2 and 75% duty cycle was administered to individual wells using 1 MHz probe of Sonidel SP 100 sonoporator for 30 s. After the US treatment, spent media was immediately discarded followed by PBS washing and fixation in 10% formaldehyde. Post fixation, the coverslip was PBS washed and then subject to flash freezing in liquid nitrogen. After freezing, the coverslip was observed under a scanning electron microscope (Cryo-FEG-SEM), and the cell surface was scanned for the presence of sonopores. Cells untreated with US were used as negative controls.

4.11. US-Triggered Cellular Uptake. MiaPaCa-2 cells were seeded at a density of 10^5 cells/well on a coverslip in a 24 well plate and incubated for 24 h at 37 °C in 5% CO_2 atmosphere and 70% relative humidity. Post incubation, spent media was discarded and replaced with 1 mL fresh DMEM containing R-6G, R-6G-labeled LPs, or R-6G LP-NB conjugates in different test groups. The relative concentration of R-6G was kept constant in all groups. All groups were evaluated with and without exposure to US. The US-treated groups were exposed to an US pulse of 1 W/cm^2 and 75% duty cycle using 1 MHz probe of Sonidel SP 100 sonoporator for 30 s. Post treatment, the plates were incubated for 3 h at 37 °C in 5% CO_2 atmosphere and 70% relative humidity. After 3 h, spent media was discarded, followed by PBS washing and fixation in 10% formaldehyde followed by PBS washes. The coverslips were glycerol mounted on glass slides and visualized under 63× objective in a confocal laser scanning microscope using excitation−emission wavelengths of 524/547 nm.

4.12. In Vitro Cytotoxicity. MiaPaCa-2, Panc-1, MDA-MB-231, and AW-8507 cells were seeded at a density of 5000 cells/well in a 96-well plate and incubated for 24 h at 37 °C in 5% CO_2 atmosphere and 70% relative humidity. Post incubation, spent media was discarded and replaced with 200 μL fresh DMEM containing ABRAXANE (group 1), PACLITAX (group 2), paclitaxel API (group 3), PTXLps (group 4), and NB-PTXLp conjugates (group 5 and 6). A PTX concentration range of 100 pM to 10 μM was used in all groups. Group 6 was treated with an US pulse of 1 W/cm^2 and 75% duty cycle using 1 MHz probe of Sonidel SP 100 sonoporator for 30 s. Post treatment, the plates were incubated for 48 h at 37 °C in 5% CO_2 atmosphere and 70% relative humidity. After 48 h, spent media was discarded and MTT assay was performed to determine the cell viability. IC_{50} values of PTX in group 1−6 were determined using Graph Pad Prism 5.0.

4.13. Statistical Analysis. All experimental studies were carried out in triplicates (n = 3), and the data obtained are represented as a combination of mean and standard deviation (mean ± standard deviation). Statistical significance was determined by students t-test, and one way and two way ANOVA using Graph Pad prism 5.0. $p < 0.05$ was considered to be statistically significant for all of the data sets.

■ ASSOCIATED CONTENT

Supporting Information

The Supporting Information is available free of charge on the ACS Publications website at DOI: 10.1021/acsomega.9b01924.

Dynamic light scattering size distribution plots; biocompatibility of NBs and Lps on L929 murine fibroblast cells; echogenic response of NBs; time point echogenicity of NBs; fitted curve IC_{50} plots; and IC_{50} evaluation (PDF)

■ AUTHOR INFORMATION

Corresponding Author

*E-mail: rinti@iitb.ac.in. Phone: +91-22-2576-7868.

ORCID

Rinti Banerjee: 0000-0002-6978-6131

Funding

Samsung Global Research Outreach (GRO) program.

Notes

The authors declare no competing financial interest.

The photos in the figures are original and unpublished, and were taken by A.P.

■ ACKNOWLEDGMENTS

The authors wish to acknowledge Industrial Research & Consultancy centre (IRCC), IITB and Sophisticated Analytical Instruments Facility (SAIF), IITB for allowing usage of the central instrumentation facility. The authors also wish to acknowledge Dr. Nitin Chaubal, Dr. Ameya Mahajan, and Dr. Bhavin Patel, Thane Ultrasound Centre for US imaging related assistance.

■ REFERENCES

(1) Breen, S.; Kofoed, S.; Ritchie, D.; Dryden, T.; Maguire, R.; Kearney, N.; Aranda, S. Remote real-time monitoring for chemotherapy side-effects in patients with blood cancers. *Collegian* **2017**, *24*, 541−549.

(2) Cosgrove, C. M.; Salani, R. Ovarian effects of radiation and cytotoxic chemotherapy damage. *Best Pract. Res. Clin. Obstet. Gynaecol.* **2019**, *55*, 37−48.

(3) Iijima, Y.; Yamada, M.; Endo, M.; Sano, M.; Hino, S. Dysgeusia in patients with cancer undergoing chemotherapy. *J. Oral Maxillofac. Surg., Med. Pathol.* **2019**, *31*, 214.

(4) Monsuez, J.-J.; Charniot, J.; Vignat, N.; Artigou, J. Cardiac side-effects of cancer chemotherapy. *Int. J. Cardiol.* **2010**, *144*, 3−15.

(5) Qin, S.-Y.; Cheng, Y.; Lei, Q.; Zhang, A.; Zhang, X. Combinational strategy for high-performance cancer chemotherapy. *Biomaterials* **2018**, *171*, 178−197.

(6) Tao, J. J.; Visvanathan, K.; Wolff, A. C. Long term side effects of adjuvant chemotherapy in patients with early breast cancer. *Breast* **2015**, *24*, S149−S153.

(7) Evans, E. R.; Bugga, P.; Asthana, V.; Drezek, R. Metallic nanoparticles for cancer immunotherapy. *Mater. Today* **2018**, *21*, 673−685.

DOI: 10.1021/acsomega.9b01924
ACS Omega 2019, 4, 15567−15580

(8) Mottaghitalab, F.; Farokhi, M.; Fatahi, Y.; Atyabi, F.; Dinarvand, R. New insights into designing hybrid nanoparticles for lung cancer : Diagnosis and treatment. *J. Controlled Release* **2019**, *295*, 250−267.
(9) Parvanian, S.; Mojtaba, S.; Aghashiri, M. Multifunctional nanoparticle developments in cancer diagnosis and treatment. *Sens. Bio-Sens. Res.* **2017**, *13*, 81−87.
(10) Pan, Y.; Xue, P.; Liu, S.; Zhang, L.; Guan, Q.; Zhu, J. Metal-Based Hybrid Nanoparticles as Radiosensitizers in Cancer Therapy. *Colloid Interface Sci. Commun.* **2018**, *23*, 45−51.
(11) Yoon, H. Y.; Selvan, S.; Yang, Y.; Kim, M.; Yi, D.; Kwon, I.; Kim, K. Engineering nanoparticle strategies for effective cancer immunotherapy. *Biomaterials* **2018**, *178*, 597−607.
(12) Boissenot, T.; Bordat, A.; Fattal, E.; Tsapis, N. Ultrasound-triggered drug delivery for cancer treatment using drug delivery systems: From theoretical considerations to practical applications. *J. Controlled Release* **2016**, *241*, 144−163.
(13) Dariva, C. G.; Coelho, J. F. J.; Serra, A. C. Near infrared light-triggered nanoparticles using singlet oxygen photocleavage for drug delivery systems. *J. Controlled Release* **2019**, *294*, 337−354.
(14) Kalhapure, R. S.; Renukuntla, J. Thermo- and pH dual responsive polymeric micelles and nanoparticles. *Chem.-Biol. Interact.* **2018**, *295*, 20−37.
(15) Kang, T.; Li, F.; Baik, S.; Shao, W.; Ling, D.; Hyeon, T. Surface design of magnetic nanoparticles for stimuli-responsive cancer imaging and therapy. *Biomaterials* **2017**, *136*, 98−114.
(16) Kim, C. S.; Duncan, B.; Creran, B.; Rotello, V. M. Triggered nanoparticles as therapeutics. *Nano Today* **2013**, *8*, 439−447.
(17) Moreira, A. F.; Dias, D. R.; Correia, I. Stimuli-responsive mesoporous silica nanoparticles for cancer therapy: A review. *Microporous Mesoporous Mater.* **2016**, *236*, 141.
(18) Moros, M.; Lopez, J.; Asin, L.; Antolin, E.; Beola, L.; Grazu, V.; Fratila, R.; Gutierrez, L.; Fuente, J. Triggering antitumoural drug release and gene expression by magnetic hyperthermia. *Adv. Drug Delivery Rev.* **2019**, *138*, 326.
(19) Mura, S.; Nicolas, J.; Couvreur, P. Stimuli-responsive nanocarriers for drug delivery. *Nat. Mater.* **2013**, *12*, 991−1003.
(20) Bi, H.; Han, X. Magnetic field triggered drug release from lipid microcapsule containing lipid-coated magnetic nanoparticles. *Chem. Phys. Lett.* **2018**, *706*, 455−460.
(21) Gao, J.; Yu, B.; Li, C.; Xu, M.; Cao, Z.; Xie, X.; Wang, W.; Liu, J. Ultrasound triggered phase-change nanodroplets for doxorubicin prodrug delivery and ultrasound diagnosis: An in vitro study. *Colloids Surf., B* **2019**, *174*, 416−425.
(22) Ninomiya, K.; Yamashita, T.; Tanabe, Y.; Imai, M.; Takahashi, K.; Shimizu, N. Targeted and ultrasound-triggered cancer cell injury using perfluorocarbon emulsion-loaded liposomes endowed with cancer cell-targeting and fusogenic capabilities. *Ultrason. Sonochem.* **2016**, *28*, 54−61.
(23) Saleh, T.; Soudi, T.; Shojaosadati, S. A. Redox responsive curcumin-loaded human serum albumin nanoparticles: Preparation, characterization and in vitro evaluation. *Int. J. Biol. Macromol.* **2018**, *114*, 759−766.
(24) Shen, S.; Li, Y.; Xiao, Y.; Zhao, Z.; Zhang, C.; Wang, J.; Li, H.; Liu, F.; He, N.; Yuan, Y.; Lu, Y.; Guo, S.; Wang, Y.; Liao, W.; Liao, Y.; Chen, Y.; Bin, J. Folate-conjugated nanobubbles selectively target and kill cancer cells via ultrasound-triggered intracellular explosion. *Biomaterials* **2018**, *181*, 293−306.
(25) Biswas, S.; Das, J.; Barman, S.; Shah, S. S.; Gangopadhyay, M.; Maiti, T. K.; Singh, N. D. P. Single component image guided "On-demand" drug delivery system for early stage prostate cancer. *Sens. Actuators, B* **2017**, *244*, 327−333.
(26) Centelles, M. N.; Wright, M.; So, P.-W.; Amrahli, M.; Xu, X. Y.; Stebbing, J.; Miller, A. D.; Gedroyc, W.; Thanou, M. Image-guided thermosensitive liposomes for focused ultrasound drug delivery: Using NIRF-labelled lipids and topotecan to visualise the effects of hyperthermia in tumours. *J. Controlled Release* **2018**, *280*, 87−98.
(27) Guo, Y.; Wang, X.-Y.; Chen, Y.-L.; Liu, F.-Q.; Tan, M.-X.; Ao, M.; Yu, J.-H.; Ran, H.-t.; Wang, Z.-X. A light-controllable specific drug delivery nanoplatform for targeted bimodal imaging-guided photo-thermal/chemo synergistic cancer therapy. *Acta Biomater.* **2018**, *80*, 308−326.
(28) Wei, C.; Dong, X.; Zhang, Y.; Liang, J.; Yang, A.; Zhu, D.; Liu, T.; Kong, D.; Lv, F. Simultaneous fluorescence imaging monitoring of the programmed release of dual drugs from a hydrogel-carbon nanotube delivery system. *Sens. Actuators, B* **2018**, *273*, 264−275.
(29) Yang, J.; Zhai, S.; Qin, H.; Yan, H.; Xing, D.; Hu, X. NIR-controlled morphology transformation and pulsatile drug delivery based on multifunctional phototheranostic nanoparticles for photo-acoustic imaging-guided photothermal-chemotherapy. *Biomaterials* **2018**, *176*, 1−12.
(30) Wischhusen, J.; Padilla, F. Ultrasound Molecular Imaging with Targeted Microbubbles for Cancer Diagnostics: From Bench to Bedside. *IRBM* **2019**, *40*, 3−9.
(31) Wischhusen, J.; Padilla, F.; Bérard, C. L. Ultrasound-Targeted Microbubble Destruction (UTMD) for Localized Drug Delivery into Tumor Tissue. *IRBM* **2019**, *40*, 10−15.
(32) Wang, D.; Yang, K.; Gao, Y.-H.; Tan, K.-B.; Liu, Z. Preparation and characterization of a nanoscale ultrasound contrast agent. *Clin. Imaging* **2010**, *34*, 288−292.
(33) Hernot, S.; Klibanov, A. L. Microbubbles in ultrasound-triggered drug and gene delivery. *Adv. Drug Deliv. Rev.* **2008**, *60*, 1153−1166.
(34) van Wamel, A.; Kooiman, K.; Harteveld, M.; Emmer, M.; Cate, F. J.; Versluis, M.; Jong, N. Vibrating microbubbles poking individual cells : Drug transfer into cells via sonoporation. *J. Controlled Release* **2006**, *112*, 149−155.
(35) Basta, G.; Venneri, L.; Lazzerini, G.; Pasanisi, E.; Pianelli, M.; Vesentini, N.; Delturco, S.; Kusmic, C.; Picano, E. In vitro modulation of intracellular oxidative stress of endothelial cells by diagnostic cardiac ultrasound. *Cardiovasc. Res.* **2003**, *58*, 156−161.
(36) Dijkmans, P.; Juffermans, L.; Musters, R.; Vanwamel, A.; Tencate, F.; Vangilst, W.; Visser, C.; Dejong, N.; Kamp, O. Microbubbles and ultrasound: from diagnosis to therapy. *Eur. J. Echocardiogr.* **2004**, *5*, 245−256.
(37) Lentacker, I.; De Cock, I.; Deckers, R.; De Smedt, S. C.; Moonen, C. T. W. Understanding ultrasound induced sonoporation: Definitions and underlying mechanisms. *Adv. Drug Delivery Rev.* **2014**, *72*, 49−64.
(38) Dimcevski, G.; Kotopoulis, S.; Bjånes, T.; Hoem, D.; Schjøtt, J.; Gjertsen, B. T.; Biermann, M.; Molven, A.; Sorbye, H.; McCormack, E.; Postema, M.; Gilja, O. H. A human clinical trial using ultrasound and microbubbles to enhance gemcitabine treatment of inoperable pancreatic cancer. *J. Controlled Release* **2016**, *243*, 172−181.
(39) Cochran, M. C.; Eisenbrey, J.; Ouma, R. O.; Soulen, M.; Wheatley, M. A. Doxorubicin and paclitaxel loaded microbubbles for ultrasound triggered drug delivery. *Int. J. Pharm.* **2011**, *414*, 161−170.
(40) Cool, S. K.; Geers, B.; Roels, S.; Stremersch, S.; Vanderperren, K.; Saunders, J. H.; De Smedt, S. C.; Demeester, J.; Sanders, N. N. Coupling of drug containing liposomes to microbubbles improves ultrasound triggered drug delivery in mice. *J. Controlled Release* **2013**, *172*, 885−893.
(41) Min, H. S.; Son, S.; You, D. G.; Lee, T. W.; Lee, J.; Lee, S.; Yhee, J. Y.; Lee, J.; Han, M. H.; Park, J. H.; Kim, S. H.; Choi, K.; Park, K.; Kim, K.; Kwon, I. C. Chemical gas-generating nanoparticles for tumor-targeted ultrasound imaging and ultrasound-triggered drug delivery. *Biomaterials* **2016**, *108*, 57−70.
(42) Haley, B.; Frenkel, E. Nanoparticles for drug delivery in cancer treatment. *Urol. Oncol.* **2008**, *26*, 57−64.
(43) Chandan, R.; Banerjee, R. Pro-apoptotic liposomes-nanobubble conjugate synergistic with paclitaxel: A platform for ultrasound responsive image-guided drug delivery. *Sci. Rep.* **2018**, *8*, 1−15.
(44) Ezrahi, S.; Aserin, A.; Garti, N. Basic principles of drug delivery systems - the case of paclitaxel. *Adv. Colloid Interface Sci.* **2019**, *263*, 95−130.
(45) Han, S.-M.; Baek, J.-S.; Kim, M.-S.; Hwang, S.-J.; Cho, C.-W. Surface modification of paclitaxel-loaded liposomes using d-α-tocopheryl polyethylene glycol 1000 succinate: Enhanced cellular

DOI: 10.1021/acsomega.9b01924
ACS Omega 2019, 4, 15567−15580

uptake and cytotoxicity in multidrug resistant breast cancer cells. *Chem. Phys. Lipids* **2018**, *213*, 39−47.
(46) Ling, L.; Du, Y.; Ismail, M.; He, R.; Hou, Y.; Fu, Z.; Zhang, Y.; Yao, C.; Li, X. Self-assembled liposomes of dual paclitaxel-phospholipid prodrug for anticancer therapy. *Int. J. Pharm.* **2017**, *526*, 11−22.
(47) Nanda, B.; Manjappa, A. S.; Chuttani, K.; Balasinor, N. H.; Mishra, A. K.; Ramachandra Murthy, R. S. Acylated chitosan anchored paclitaxel loaded liposomes: Pharmacokinetic and biodistribution study in Ehrlich ascites tumor bearing mice. *Int. J. Biol. Macromol.* **2019**, *122*, 367−379.
(48) McIlvain, G.; Ganji, E.; Cooper, C.; Killian, M. L.; Ogunnaike, B. A.; Johnson, C. L. Reliable preparation of agarose phantoms for use in quantitative magnetic resonance elastography. *J. Mech. Behav. Biomed. Mater.* **2019**, *97*, 65−73.

DOI: 10.1021/acsomega.9b01924
ACS Omega 2019, 4, 15567−15580